

# Alleviating Class-wise Gradient Imbalance for Pulmonary Airway Segmentation

Hao Zheng, Yulei Qin, *Student Member, IEEE*, Yun Gu, *Member, IEEE*, Fangfang Xie, Jie Yang, Jiayuan Sun, Guang-Zhong Yang, *Fellow, IEEE*

arXiv:2011.11952v1 [eess.IV] 24 Nov 2020

**Abstract**— Automated airway segmentation is a prerequisite for pre-operative diagnosis and intra-operative navigation for pulmonary intervention. Due to the small size and scattered spatial distribution of peripheral bronchi, this is hampered by severe class imbalance between foreground and background regions, which makes it challenging for CNN-based methods to parse distal small airways. In this paper, we demonstrate that this problem is arisen by gradient erosion and dilation of the neighborhood voxels. During back-propagation, if the ratio of the foreground gradient to background gradient is small while the class imbalance is local, the foreground gradients can be eroded by their neighborhoods. This process cumulatively increases the noise information included in the gradient flow from top layers to the bottom ones, limiting the learning of small structures in CNNs. To alleviate this problem, we use group supervision and the corresponding WingsNet to provide complementary gradient flows to enhance the training of shallow layers. To further address the intra-class imbalance between large and small airways, we design a General Union loss function which obviates the impact of airway size by distance-based weights and adaptively tunes the gradient ratio based on the learning process. Extensive experiments on public datasets demonstrate that the proposed method can predict the airway structures with higher accuracy and better morphological completeness.

**Index Terms**— Airway segmentation, class imbalance, gradient erosion and dilation, group supervision, General Union loss

## I. INTRODUCTION

Airway segmentation from computed tomography (CT) scans is used in a wide range of diagnostic and interventional procedures for lung diseases. As manual annotation is laborious, time-consuming and requires extensive clinical and image

This work was partly supported by National Key R&D Program of China (2019YFB1311503), Committee of Science and Technology, Shanghai, China (19510711200), Shanghai Sailing Program (20YF1420800), NSFC (61661010, 61977046, 62003208). (Corresponding authors: Jie Yang; Jiayuan Sun.)

Hao Zheng, Yulei Qin, Yun Gu, Jie Yang and Guang-Zhong Yang are with the Institute of Medical Robotics, Shanghai Jiao Tong University, Shanghai, China. (e-mail: jieyang@sjtu.edu.cn)

Hao Zheng, Yulei Qin, Yun Gu and Jie Yang are with the Institute of Image Processing and Pattern Recognition, Shanghai Jiao Tong University, Shanghai, China.

Hao Zheng and Guang-Zhong Yang are with the School of Biomedical Engineering, Shanghai Jiao Tong University, Shanghai, China.

Fangfang Xie and Jiayuan Sun are with the Department of Respiratory and Critical Care Medicine, Department of Respiratory Endoscopy, Shanghai Chest Hospital, Shanghai, China. (e-mail: jy-sun1976@163.com)

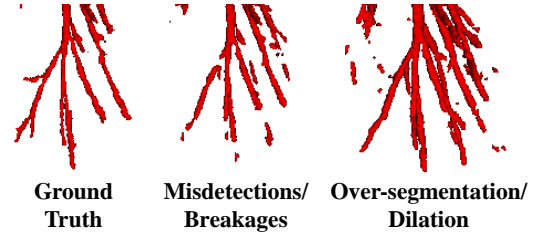


Fig. 1. Illustration of the impacts of inter-class imbalance. Without larger weights for airway voxels in the loss function, the trained network may fail to segment a complete branch. In contrast, a large weight helps to detect more complete bronchi while the predicted branches are thicker than the ground truth. A part of the airway wall is misclassified as lumen.

interpretation experience, automatic airway segmentation can reduce the manual efforts and accelerate the reconstruction of pulmonary structures. In recent years, deep learning methods have been widely used in medical image analysis. As for automatic airway segmentation, many existing efforts [6], [17], [20], [29], [35], [36] adopt convolutional neural networks (CNNs) to learn robust and discriminative features. The major challenge in this task is to accurately reconstruct complete airway tree branches, which needs a high sensitivity of distal small airways. Due to the small size and scattered spatial distribution of peripheral bronchi, the segmentation accuracy is degraded by severe class imbalance. In this paper, we demonstrate the intrinsic impact of class imbalance on the training of CNNs and propose method to deal with this problem.

For airway segmentation, the first kind of class imbalance is that the number of airway voxels is far fewer than that of background, which is denoted by **inter-class imbalance** in this paper. As shown in Fig. 1, if we ignore the influence of inter-class imbalance in a segmentation pipeline, the performance will be limited by misdetections and breakages of small airway branches. By assigning larger weights to the airway voxels in the loss function, more complete branches can be detected. However, their diameters can be larger than the ground truth since a part of airway wall is misclassified as lumen. We demonstrate that this phenomenon in airway segmentation can be interpreted as the **gradient erosion and dilation** of the neighborhood, which is directly caused by the inter-class imbalance. As shown in Fig. 2, if the magnitude of the gradients to small airway points is not much larger than those of the background points, their gradients may be eroded

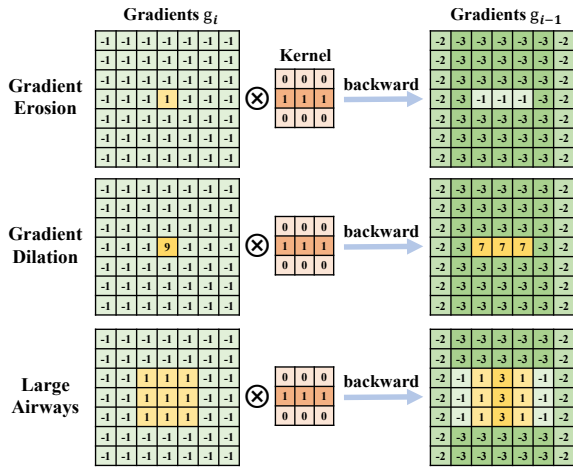


Fig. 2. Illustration of gradient erosion and dilation. For distal airways, the small foreground gradients may be eroded by the surrounding background gradients during backpropagation, while the large foreground gradients can inversely affect their background neighborhoods. For large airways, this problem is not serious.

by the surrounding background gradients via convolutional kernels. Moreover, this process is cumulative and the sign of gradients can be changed during backpropagation. As a result, the shallow layers do not learn to recognize these peripheral bronchi. After assigning larger weights to these points, the large gradients will inversely affect their background neighborhoods, leading to the dilation issue. In this case, the network tends to classify the surrounding background voxels as foreground. Such dilation may cause leakages especially at bifurcations. In contrast, the voxels in thick branches have more foreground neighbors, which protect them from erosion. Actually, the gradient erosion and dilation caused by inter-class imbalance is an inherent property of CNNs, while it can be mitigated by supervision that enhances the training of shallow layers.

Another kind of class imbalance is **intra-class imbalance**, which refers to the relative total volume difference of trachea, main bronchi, lobar bronchi and distal segmental bronchi. Large airways account for the majority of the total volume, and for data-driven algorithms, such imbalanced distribution affects the segmentation performance of peripheral bronchi. In this paper, we use Dice Loss [18] as an example to analyze the intra-class imbalance in segmentation. The Dice loss is defined as follows:

$$D = 1 - \frac{2 \times \sum_{i=1}^N p_i g_i}{\sum_{i=1}^N p_i + \sum_{i=1}^N g_i}, \quad (1)$$

where  $N$  is the total number of voxels,  $p_i$  is the prediction of each voxel and  $g_i$  is the corresponding ground truth. In this loss, the same gradients are given to all foreground or background locations ( $\frac{\partial D}{\partial p_i} = \frac{\partial D}{\partial p_j}$  if  $g_i = g_j$ )<sup>1</sup>. For further analysis with regard to the gradient erosion and dilation, we calculate the ratio of the foreground gradient  $\frac{\partial D}{\partial p_f}$  to

background gradient  $\frac{\partial D}{\partial p_b}$ ,

$$r_{Dice} = \left| \frac{\partial D}{\partial p_f} / \frac{\partial D}{\partial p_b} \right| = \frac{2}{1-D} - 1. \quad (2)$$

This proportion is in inverse ratio to the Dice similarity coefficient (DSC). During training, if an input patch includes both small and large airways, the total DSC is high as the large airways are not seriously influenced by the inter-class imbalance. This leads to small  $r_{Dice}$  which aggravates the gradient erosion, thus affecting the learning of small airways. To deal with this problem, the design of loss function plays a vital role.

In this paper, we address the inter-class and intra-class imbalance from the aspects of supervision manner and loss function respectively. As a major reason for gradient erosion and dilation is the successive stack of convolutional layers, in previous works, deep supervision [30] adds more decoding paths after several middle layers. These supplementary supervisions provide complementary gradients for the bottom part of the network. However, within each encode-decode path, the defective information is still cumulated. To reduce this negative impact, we develop a new supervision flow named group supervision which directly transforms complementary gradients to each convolutional block (ConvBlock). In group supervision, the ConvBlocks are divided into different groups with respective loss functions. Feature pyramid is built within each group and delivers nearly original gradients to all the members. WingsNet is built by integrating the group supervision with an UNet [7] structure to learn the detailed representations of small targets under severe inter-class imbalance. For intra-class imbalance, it is necessary to modify the gradients of different airway voxels. On the one hand, the segmentation of thick branches does not need a large gradient ratio, which is the key to learn the representations of peripheral bronchi. On the other hand, some branches are close to the vessels or lesions, making it harder to be detected. To this end, we propose a General Union loss that assigns distance-based weights to different airway voxels and further increases the gradient ratios of the hard-to-segment regions.

The main contributions of this work are as follows:

- 1) Gradient erosion and dilation are first introduced to elucidate the influence of class imbalance when adopting CNNs in segmentation. Extensive experiments on two public datasets demonstrate the efficacy of our method.
- 2) A novel supervision flow is developed to enhance the training of shallow layers under severe inter-class imbalance. WingsNet is built by combining the proposed group supervision with an encode-decode structure.
- 3) General Union loss is proposed to deal with the intra-class imbalance via distance-based weights and element-wise focus on the hard-to-segment regions.

## II. RELATED WORK

### A. Airway Segmentation

Thus far, many methods have been proposed for airway segmentation. In 2009, fifteen algorithms (ten fully automatic and five semi-automatic) were compared in a segmentation

<sup>1</sup>Detailed analysis can be found in the supplementary material.

challenge (EXACT’09 [16]). Conventional methods such as region growing [19], template matching [4] and gradient vector flow [3] are adopted and thick tubular structures (trachea, principle bronchi, etc.) can be well detected in these works. However, due to the lack of semantic features, the blurred or broken airway walls limit their performance in terms of peripheral bronchi.

In recent years, deep learning methods are widely used in this task [6], [17], [20], [29], [35], [36]. Some papers directly use 3D segmentation neural networks to get the final segmentation results. Juarez *et al.* [14] adopt 3D UNet as their segmentation network while Qin *et al.* [20] propose AirwayNet which emphasizes the connectivity of voxels. Deep neural networks are also cooperated with conventional methods. Jin *et al.* [12] first train a 3D fully convolutional network (FCN) followed by a graph-based refinement. Zhao *et al.* [36] separately train their 3D and 2D networks, then perform linear programming to combine these results. Besides, CNNs are integrated in a tracking framework. Yun *et al.* [35] use 2.5D CNN to classify the candidates generated based on the segmentation masks in the previous iteration. Meng *et al.* [17] track the airways along the centerlines and adopt 3D UNet to extract the airways in the volume of interest. However, the class imbalance which plays a vital role in accurate distal bronchi segmentation has not been thoroughly discussed. In this paper, we especially focus on this problem and propose the corresponding solutions.

### B. Class Imbalance in Image Segmentation

The approaches to mitigate the class imbalance in segmentation can be divided into two categories, the sampling strategies and the cost-sensitive learning techniques. In 3D image segmentation, the widely used two-stage framework consisting of a localization phase and a refinement stage can be seen as an over-sampling method for the minority class. Wang *et al.* [32] propose a sampling policy, named Relaxed Upper Confident Bound to deal with the trade-off between exploitation and exploration in multi-organ segmentation. In the cost-sensitive learning techniques, Tversky loss [24] and Generalized Dice loss [27] can be used to boost the sensitivity of under-represented class. Besides, focal Dice loss [31], focal Tversky loss [1] and exponential logarithmic loss [33] achieve a patch-wise focus function by changing the root of the union-based losses (Dice loss, Tversky loss, etc.). Moreover, prior knowledge in a certain task is also integrated into the loss function design [29]. To deal with the intra-class imbalance between large and small airways, in this paper, we incorporate the airway-tree prior knowledge as well as the element-wise focal function which assigns larger gradients to the hard-to-segment voxels.

## III. METHODS

### A. Overview

Our framework is effective and robust for airway segmentation. During training, the input patches are sampled from the CT scans via a hard skeleton sampling strategy. The proposed WingsNet is built with group supervision and trained by Root

Tversky loss and General Union loss. During testing, the trained WingsNet takes small patches as input by a sliding window manner. The following sections provide a detailed explanation of the group supervision, WingsNet and General Union loss.

### B. Group Supervision

Under severe class imbalance, the stack of convolutional layers (ConvLayers) is a major reason for the gradient erosion and dilation problem. However, it is ineffective to deal with this by reducing the depth of the network, since this also weakens the representative ability of the model. Instead, as this problem mainly affects the training of shallow layers, we can take measures to reduce the noisy information included in the gradients when arriving these parts. In this paper, we propose a novel supervision manner named group supervision with its corresponding network architecture called WingsNet to achieve this purpose.

In previous works, Deep supervision [30] generates extra encode-decode paths while within each path, the stack of layers still leads to the gradient erosion and dilation. Deeply supervised nets [15] impose loss functions on each ConvBlock, but such dense supervision may have side effect on the learning of hierarchical representations if the shallow and middle layers are also forced to generate a segmentation only based on their own features. To provide complemental gradients to each block while preserving the hierarchical representations, we propose to separate the ConvBlocks into different group while supervising each of them. Fig. 3 demonstrates an example of group supervision. Twenty one ConvBlocks are divided into 4 groups in a cross manner. Within each group, the prediction is made based on a feature pyramid which is a concatenation of the features from their member blocks. To build this pyramid, each block has an additional path consisting of a  $1 \times 1 \times 1$  ConvLayer followed by an up-sampling operation. It should be noticed that the  $1 \times 1 \times 1$  ConvLayer does not contribute to gradient erosion and dilation, thus the gradients from this path can help the middle layers to learn the representation of small structures. More generally, the number of groups is variable according to the network property. And the partition of groups is also not fixed while it is important to keep a hierarchical representation within each group. Different kinds of group supervision manners are compared in our experiment. Finally, for the  $i^{th}$  group, the binary segmentation can be obtained by

$$P_i = \text{Sigmoid}(\text{Conv1}(\text{Cat}(f_{i,1}, f_{i,2}, \dots, f_{i,n}))), \quad (3)$$

where ‘Conv1’ denotes  $1 \times 1 \times 1$  convolution, ‘Cat’ means concatenation,  $f_{i,j}$  denotes the features from the  $j^{th}$  block and  $n$  is the total number of blocks in this group.

To adopt the proposed group supervision in airway segmentation, we build the WingsNet with similar architecture as shown in Fig. 3. The only difference is that in WingsNet, there are only two groups, where the ConvBlocks belonging to encoding path (ConvBlock 1-12) are divided into one group and the decoding path (ConvBlock 13-18) forms another. For the  $i^{th}$  ConvBlock, its outputs to the next block  $f_{b,i}$  and the

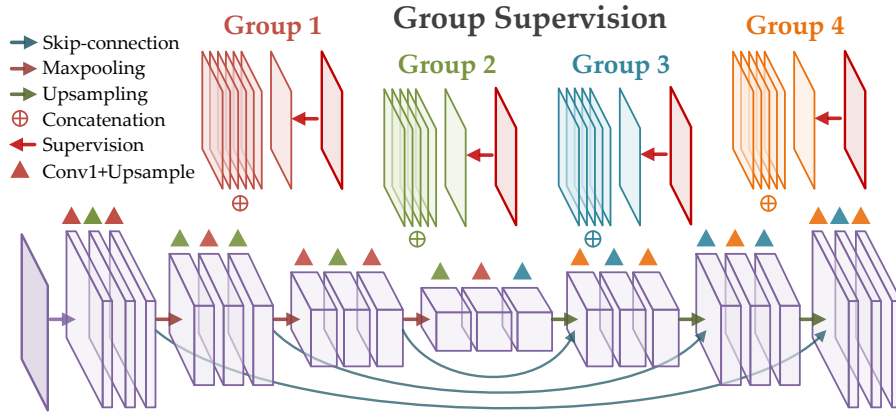


Fig. 3. This figure illustrates an example of group supervision, in which the ConvBlocks are divided into four groups according to the color of triangles. In each ConvBlock, there are two output paths, one to the next block and another to the group feature pyramid. The second path consists of a  $1 \times 1 \times 1$  ConvLayer (‘Conv1’) and an upsampling layer. Supervisions are imposed on each group.

group feature pyramid  $f_{g,i}$  are obtained by

$$f_i^0 = \text{ReLU}(\text{IN}(\text{Conv3}(f_{b,i-1}))), \quad (4)$$

$$f_i^1 = \text{Sigmoid}(\text{Conv1}(f_{0,i})) \odot f_{0,i}, \quad (5)$$

$$f_{b,i} = \text{Sigmoid}(\text{Conv1}(f_{1,i})) \odot f_{1,i}, \quad (6)$$

$$f_{g,i} = \text{Upsample}(\text{Conv1}(f_{b,i})), \quad (7)$$

where  $f_{b,i-1}$  is output of the previous block,  $f_i^0$  and  $f_i^1$  are intermediate results, ‘IN’ is instance normalization,  $\odot$  is Hadamard product, and ‘Conv3’ means  $3 \times 3 \times 3$  convolution. As the inter-class imbalance problem stems from the large number of background points, it can be mitigated via adaptively suppressing the background locations during training. We achieved this by spatial attention module [23], which generates a soft mask applied on  $f_{0,i}$ . Moreover, we cascade two modules to generate the attention map in a coarse-to-fine manner. But limited by the capacity of GPU memory, the first three and last two ConvBlocks only include the one-stage original spatial attention module. In addition, we adopt SpatialDropout [28] before the last  $1 \times 1 \times 1$  convolution within each group for regularization.

### C. General Union Loss

In medical imaging, union-based losses such as Dice loss and Tversky loss [24] are widely used to address the class imbalance problem. As shown in (21), Dice loss can adaptively change the gradient ratio according to the segmentation performance, resulting in an increased sensitivity for the minority class. However, due to the intra-class imbalance, the network trained by Dice loss may not learn to detect the distal bronchi. To improve the airway tree length detected, we can impose a lower bound to the gradient ratio, preventing the gradient erosion problem. This can be achieved by weighted Dice loss and Tversky loss.

For weighted Dice loss,

$$D_w = 1 - \frac{2 \times \sum_{i=1}^N w_i p_i g_i}{\sum_{i=1}^N w_i (p_i + g_i)}, \quad (8)$$

similar to Dice loss, the same gradients are given to all foreground or background voxels ( $\frac{\partial D_w}{\partial p_i} = \frac{\partial D_w}{\partial p_j}$  if  $g_i = g_j$ ). Its gradient ratio is

$$\left| \frac{\partial D_w}{\partial p_f} / \frac{\partial D_w}{\partial p_b} \right| = \frac{w_f}{w_b} \left( \frac{2}{1 - D_w} - 1 \right) \geq \frac{w_f}{w_b}, \quad (9)$$

where  $w_f$  and  $w_b$  are the weights for foreground and background respectively. From (24), we can find three properties of weighted Dice loss. First, its gradient ratio can be adaptively changed due to  $\frac{2}{1 - D_w} - 1$ . Second, this change is amplified by the factor  $\frac{w_f}{w_b}$ . Third, the gradient ratio has a lower bound of  $\frac{w_f}{w_b}$ . These properties make it effective to improve the segmentation of under-represented class by tuning the weights  $w_f$  and  $w_b$ . The same properties can be found in Tversky loss [24],

$$T = 1 - \frac{\sum_{i=1}^N p_i g_i}{\sum_{i=1}^N (\alpha p_i + \beta g_i)}. \quad (10)$$

where  $\alpha + \beta = 1$ . And its gradient ratio is

$$\left| \frac{\partial T}{\partial p_f} / \frac{\partial T}{\partial p_b} \right| = \frac{1}{\alpha} \frac{1}{1 - T} - 1 \geq \frac{\beta}{\alpha}. \quad (11)$$

By tuning the hyper-parameter  $\alpha$ , Tversky loss also can achieve a high sensitivity for peripheral small airways.

Despite the merits of these losses, they do not address the intra-class imbalance problem. The cost for a high tree length detected is the significant dilation problem, because the same large gradients are assigned to all foreground points. Actually, we do not need to increase the gradients to the easy-to-segment parts such as the large airways, while more attention should be paid to the hard-to-segmentation areas to improve the connectivity of the predicted bronchi. To this end, we propose a Root Tversky loss which combines the voxel-level focal function into Tversky loss, and a General Union loss is further generated by adding the distance-based weights.

Root Tversky loss achieves the element-wise focal function by changing the root of the predictions in the numerator of

<sup>2</sup>More details can be found in the supplementary material.

Tversky loss,

$$T_r = 1 - \frac{\sum_{i=1}^N p_i^r g_i}{\alpha \sum_i p_i + \beta \sum_i g_i}, \quad (12)$$

where  $0 < r < 1$  and  $\alpha + \beta = 1$ . It is differentiated in term of  $p_j$ , and the gradient is

$$\frac{\partial T_r}{\partial p_j} = - \frac{r g_j p_j^{r-1} (\alpha \sum_i p_i + \beta \sum_i g_i) - \alpha \sum_i p_i^r g_i}{(\alpha \sum_i p_i + \beta \sum_i g_i)^2}. \quad (13)$$

As  $r - 1 < 0$ , we replace  $p_i^{r-1}$  by  $(p_i + \epsilon_i)^{r-1}$  where  $\epsilon$  is a small positive number. The same gradients are given to all background voxels while  $p_j^{r-1}$  controls the gradients given to foreground locations. Since  $0 < r < 1$ , much larger gradient is given to the foreground voxel with small  $p_j$ . Its gradient ratio is

$$\left| \frac{\partial T_r}{\partial p_f} / \frac{\partial T_r}{\partial p_b} \right| = \frac{r p_{f,j}^{r-1}}{\alpha} \frac{1}{1 - T_r} - 1 \geq \frac{r}{\alpha} - 1, \quad (14)$$

where  $p_{f,j}$  is the prediction of a foreground voxel  $j$ . Comparing (28) and (31), the main difference between Tversky loss and Root Tversky loss is that the amplification factor  $\frac{1}{\alpha}$  in Tversky loss is replaced by  $\frac{r p_{f,j}^{r-1}}{\alpha}$ . In this new factor, the  $p_{f,j}^{r-1}$  item achieves the voxel-wise focal function for the hard-to-segment points, while for the easy-to-segment airway voxels, this factor is near  $\frac{r}{\alpha}$ , resulting in smaller gradient ratio and alleviating the dilation problem.

As the intra-class imbalance is caused by the large number of thick airway voxels, we can manually decrease the weights for most large airway points. In this paper, we achieve this by assigning the weights for each voxel according to their distance to the centerlines,

$$w_i = \begin{cases} 1 - m \left( \frac{d_i}{d_{max}} \right)^{r_d}, & g_i = 1 \\ 1, & g_i = 0 \end{cases} \quad (15)$$

where  $d_i$  is the shortest distance from the current location to the centerline,  $d_{max}$  is the maximum  $d_i$  in one case and  $r_d$  controls the pattern of decay. By adding this weight to Eq. (31), the loss function is in the following form:

$$U = 1 - \frac{\sum_{i=1}^N w_i p_i^r g_i}{\sum_{i=1}^N w_i (\alpha p_i + \beta g_i)}. \quad (16)$$

To reduce the number of hyper-parameters, we set  $m = \frac{1-\alpha}{\alpha}$  in  $w_i$ . Its gradient with regard to  $p_j$  is

$$\frac{\partial U}{\partial p_j} = - \frac{w_j r g_j p_j^{r-1} \sum_i w_i (\alpha p_i + \beta g_i) - w_j \alpha \sum_i w_i p_i^r g_i}{[\sum_{i=1}^N w_i (\alpha p_i + \beta g_i)]^2}. \quad (17)$$

And the gradient ratio of this loss is

$$\left| \frac{\partial U}{\partial p_f} / \frac{\partial U}{\partial p_b} \right| = w_{f,j} \left[ \frac{r p_{f,j}^{r-1}}{\alpha} \frac{1}{1 - U} - 1 \right] \geq (1 - m) \left( \frac{r}{\alpha} - 1 \right). \quad (18)$$

It is seen that the distance-based weight  $w_i$  is directly applied on the gradient ratio of each point. Besides, since the weights of most large airway voxels are decreased, small airways

play a more important role in the item  $\frac{1}{1-U}$ . In other words, the adaptive changing of gradient ratio depends more on the sensitivity of peripheral bronchi. By adopting this distance-based weight, the dilation issue around the large airways can be resolved while keeping a high tree length detected.

## IV. EXPERIMENTS AND RESULTS

### A. Dataset

We evaluated our method in two public datasets. The **EXACT'09** [16] challenge provided a training set and a test set each with 20 CT scans, while no annotation is publicly available. The **Binary Airway Segmentation Dataset** [21] included 90 CT scans (70 from LIDC [2] and 20 from the training set of the EXACT'09). The pixel spacing varied from 0.5 to 0.82 mm, and the slice thickness ranged from 0.5 to 1.0 mm. For the Binary Airway Segmentation Dataset, we randomly split the 90 scans into training set, validation set and test set with 50, 20 and 20 samples respectively. For the EXACT'09 dataset, we trained our model on the training set with the corresponding annotations from the Binary Airway Segmentation Dataset, and submitted our results on the test set for evaluation. During preprocessing, the pixel values were clamped to  $[-1000, 600]$  HU, before rescaled to  $[0, 255]$ . We also masked the background voxels outside the chest with maximal intensity.

### B. Implementation Details

During training, we sampled 16 patches with a size of  $[128, 128, 128]$  from each image in each epoch via a hard skeleton sampling strategy. The network was first trained by Dice loss and the false negatives were selected as the hard-to-segment regions. In hard skeleton sampling, We randomly selected a skeleton point belonging to those regions, and generated a patch containing it. Finally, we set a threshold  $p_s = 0.5$  to determine online for random sampling or hard sample mining during training. SGD optimizer with a momentum of 0.9 and a weight decay of 0.0001 was chosen. We further adopted a multi-stage training strategy to boost the tree length detected. A high-sensitive segmentation was obtained in the first phase, then the network was fine-tuned to gradually increase the precision. In the first stage, the network was trained by 100 epochs. The initial learning rate was 0.01, and it was divided by 10 in the 60th and 90th epoch. During the second stage, the network was further trained by 30 epochs. The initial learning rate was 0.01, and it was divided by 10 in the 15th and 25th epoch. Besides, We performed random rotation between  $[-15^\circ, 15^\circ]$  with trilinear interpolation for data augmentation. In trilinear interpolation, a threshold was used to convert the float image into binary mask. Since a large threshold (0.9) could narrow down the annotation and provide a little leeway for the dilation, they were 0.8 and 0.9 in the first and second stages. The hyperparameters were tuned in the validation set of the Binary Airway Segmentation Dataset and experiments for each hyper-parameter are shown in the supplemental material. During the first stage, we chose  $r_l = 0.7$ ,  $\alpha = 0.1$ ,  $r_d = 0.5$  and  $\epsilon = 0.0001$  in general union loss, while in the second stage, we reset  $\alpha = 0.2$ .

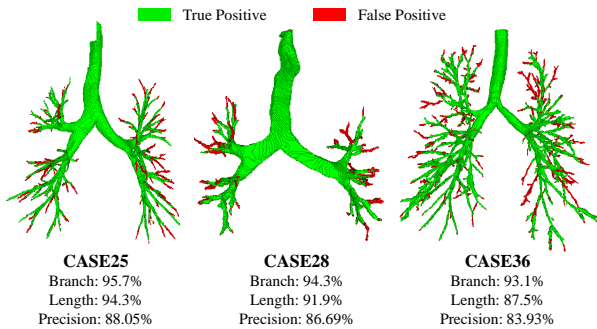


Fig. 4. Three cases with the lowest precision on the EXACT’09 dataset. Most false positives belong to unannotated distal bronchi while no significant clumping leakage is observed.

## V. SEGMENTATION RESULTS

TABLE I  
COMPARISON IN THE EXACT’09 DATASET.

Method	Branch(%)	Length(%)	Precision(%)
Irving <i>et al.</i> [11]	43.5(19.1)	36.4(17.1)	98.7(2.9)
Pinho <i>et al.</i> [19]	32.1(6.9)	26.9(6.9)	96.6(4.9)
Bauer <i>et al.</i> [3]	63.0(10.4)	58.4(13.2)	98.6(2.1)
Born <i>et al.</i> [4]	41.7(16.2)	34.5(13.2)	<b>99.6(1.1)</b>
Feuerstein <i>et al.</i> [8]	76.5(13.3)	73.3(13.4)	84.4(9.5)
Inoue <i>et al.</i> [10]	79.6(13.5)	<b>79.9(12.1)</b>	88.1(13.2)
Xu <i>et al.</i> [34]	51.7(10.8)	44.5(9.4)	99.2(1.6)
Yun <i>et al.</i> [35]	65.7(13.1)	60.1(11.9)	95.4(3.7)
Proposed	<b>80.5(12.5)</b>	79.0(11.1)	94.2(4.3)

We adopt four evaluation metrics including tree length detected rate [8], branch detected rate [8], DSC and precision. Table I illustrates the quantitative results in the EXACT’09 dataset. Among the participants of this challenge, the best branch detected (76.5%) as well as length detected (73.3%) rates were achieved by Feuerstein *et al.* [8]. They adopt a tracking framework to generate the volume of interest (VOI), and a sharpening filter is used to enhance the edges of airways, followed by a region growing method to extract the branches. A main challenge in such method is the blurry airways walls, which cause the leakages and result in a relatively low precision of 84.4%. In the following works on this dataset, Inoue *et al.* [10] utilize Hessian analysis [25] to generate the candidates, and train an AdaBoost [26] classifier to reduce the false positives before obtaining the airway tree by minimum spanning tree [9] and 3D Graph Cuts [5]. Compared with this method, we achieve the comparable branch detected (80.5%*vs.*79.6%) and tree length detected (79.0%*vs.*79.9%) with a higher precision (94.2%*vs.*88.1%). Xu *et al.* [34] combine a hybrid multi-scale fuzzy connectedness segmentation algorithm with two tubular structure enhancement techniques to extract the airway tree while Yun *et al.* [35] train a 2.5D CNN for bronchi segmentation. In comparison, we achieve higher sensitivity. Fig. 4 demonstrates three cases with the lowest precision in our segmentation results. It is seen that most false positives belong to unannotated distal bronchi while no significant clumping leakage is observed.

Table. II compares our results with other CNN-based meth-

TABLE II  
COMPARISON IN THE BINARY AIRWAY SEGMENTATION DATASET.

Method	Length(%)	Branch(%)	Precision(%)
Qin <i>et al.</i> [20]	83.6(10.4)	81.4(13.8)	95.8(1.8)
Wang <i>et al.</i> [29]	86.3(8.5)	83.5(11.2)	93.4(2.1)
Juarez <i>et al.</i> [14]	84.1(8.6)	82.1(12.4)	91.4(2.5)
Juarez <i>et al.</i> [13]	68.0(21.1)	60.5(23.9)	<b>96.4(1.8)</b>
Jin <i>et al.</i> [12]	85.4(10.4)	83.1(11.5)	93.9(1.9)
Proposed	<b>92.5(4.5)</b>	<b>88.7(7.9)</b>	91.4(3.3)

ods on the Binary Airway Segmentation dataset. Qin *et al.* [20] develop AirwayNet which predicts the connectivity of airways voxels. The prediction of connectivity improves the precision but the sensitivity is still limited since it does not explicitly mitigate the gradient erosion problem. Wang *et al.* [29] train their spatial fully connected network with radial distance loss, which places higher weights to the centerlines while reducing the weights of airway voxels far away from the centerlines, alleviating the intra-class imbalance and resulting in higher length detected (86.25%). Juarez *et al.* [14] train a 3D UNet with Dice loss and weighted binary cross entropy (wBCE) loss. The wBCE loss gives higher weights to the airway voxels, increasing the sensitivity. They also design a UNet-GNN architecture [13] by replacing the two convolutional layers in the deepest level of the 3D UNet by a Graph Neural Network module. In our experiment, we found that the GNN layers failed in several cases, resulting in much higher standard deviation (21.1%) than other methods. Jin *et al.* [12] train a 3D UNet with wBCE loss for coarse segmentation followed by graph-based refinement. The refinement contributes to both the length detected and precision. Compared with these methods, our approach can improve the tree length detected more than 6% only with a little decrease in precision. Some examples are visualized in Fig. 5, demonstrating the relative merit of the method proposed.

### A. Ablation Study

To compare different network architectures, we calculated the DSC within five airway diameter intervals. Deep supervision is inserted into all the baselines [18], [22], [23], [37] while spatial attention is adopted by ‘UNet+PE’ [22] and ‘UNet+SE’ [23]. As shown in Fig. 6, all the networks can achieve a high DSC for the thick airways. However, in the test set of Binary Airway Segmentation dataset, the branches with a diameter larger than 4mm only account for 14% of the total number. The remaining 76% of branches belong to the small airways whereas the segmentation performance drops significantly for this class. The result of our WingsNet is 2.5% higher than the baselines in the interval between 0 and 2mm, demonstrating the efficacy of group supervision for peripheral bronchi segmentation. We also compared five loss functions in the same manner and the results are shown in Fig. 7. Compared with General Union loss, Root Tversky loss does not explicitly decrease the weights of large airways, leading to a dilated segmentation and a decreased DSC for the branches with a diameter between 2mm and 8mm. In contrast, without the voxel-wise focal function, Prior Tversky loss has a lower DSC

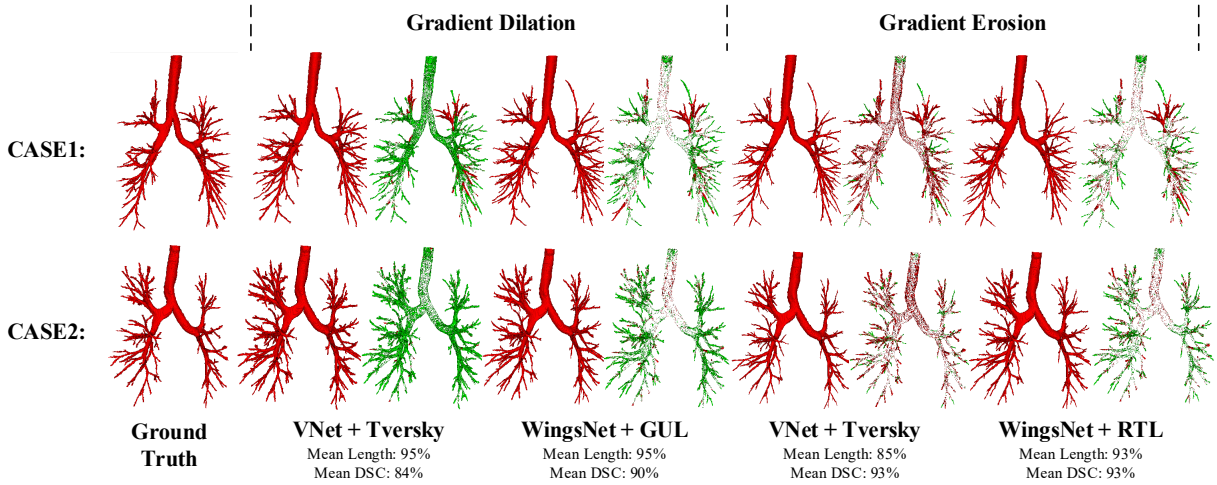


Fig. 5. The segmentation results of the proposed methods and the baseline. For each combination, the left figure is the segmentation result, while the right figure illustrates the false positives in green and the false negatives in red. With a same length detected of 95%, the dilation problem in the baseline is more serious. When we fixed the DSC to 93%, in the results of VNet, false negatives appear in the surface of airways as well as many distal bronchi. In contrast, the number of false negatives is much smaller in the results of WingsNet.

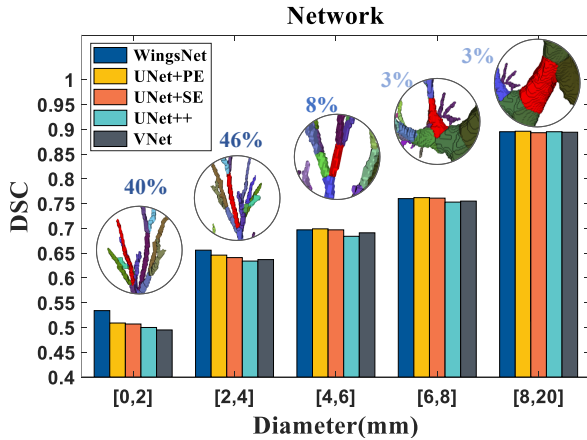


Fig. 6. The segmentation results of five networks within different airway diameter intervals. The round pictures give examples for the corresponding diameter and the percentage of branches within each interval is also labeled.

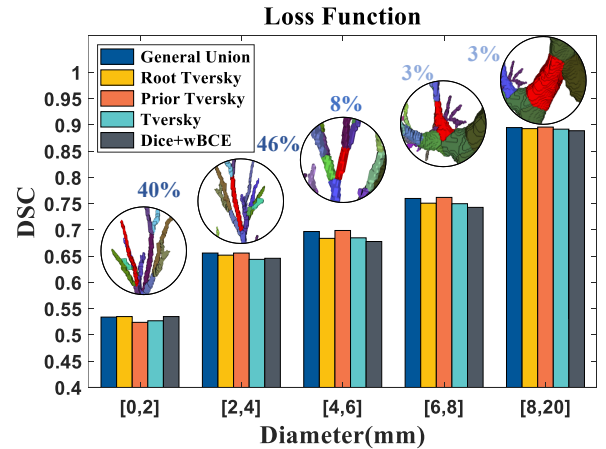


Fig. 7. The segmentation results of WingsNet trained by five loss functions. The round pictures give examples for the corresponding diameter in which the selected branch is colored in red. The percentage of branches within each interval is also labeled.

in terms of the distal small airways. The combination of Dice loss and wBCE loss can achieve a comparable performance for the peripheral bronchi. But meanwhile, the DSC is decreased for the other branches due to the dilation problem.

We further compare different supervision methods under the scenario of a high tree length detected rate. As shown in Fig. 8, adopting deep supervision can improve the length detected rate from 92.8% to 95% while keeping a comparable precision. However, supervising each ConvBlock leads to a 1.2% decrease in length detected. By dividing the blocks into two groups, with a same length detected of 95%, the precision is increased by 2.8%. When the supervision on encoding path is removed, the length detected drops about 1.4%. Besides, if all the blocks are divided into one group, the performance is even worse than deep supervision. In contrast, adding the group number to four does not affect the segmentation results significantly. Moreover, for the four groups, we separated them via a successive manner as well as a cross manner. However,

no significant difference is observed in the experiment. By these comparisons, it is shown that the segmentation of small structures benefits from the supplemental gradients while it is important to keep a hierarchical representation within each group.

## VI. DISCUSSION

### A. False Positives

The main drawback of our method is the decline in precision. Compared with some approaches, although the tree length detected improves about 6%, the decrease in precision is also more than 2%. In our segmentation results, the False Positives (FPs) can be divided into three categories and Fig. 9 illustrates six regions including FPs with their original CT images. As shown in sub-figures (a) (b) (d) (e), the largest number of FPs appear in the indistinct borders between airway lumen and airway walls. During the annotation process, observers refined the coarse segmentation obtained by region

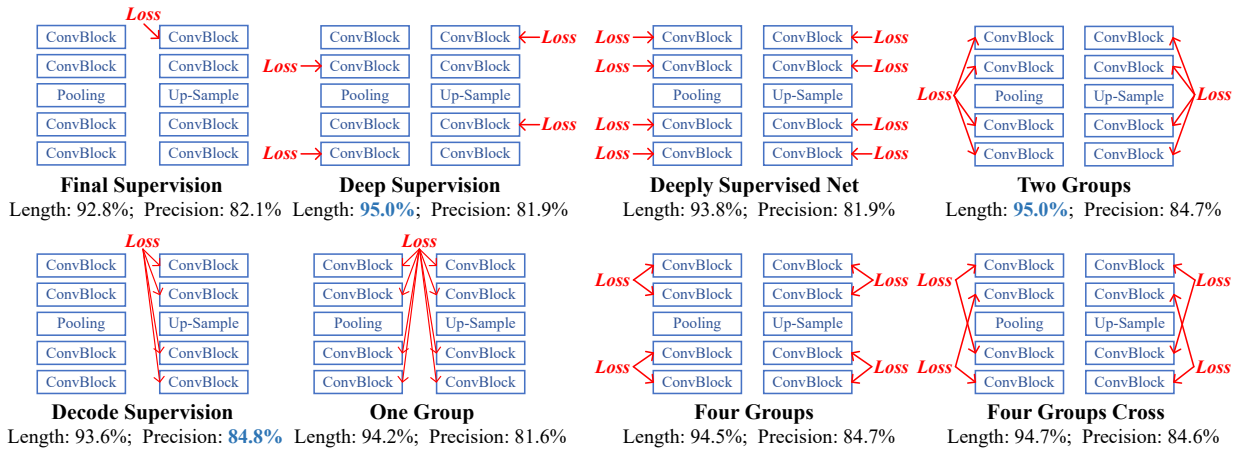


Fig. 8. Comparison of different supervision approaches.

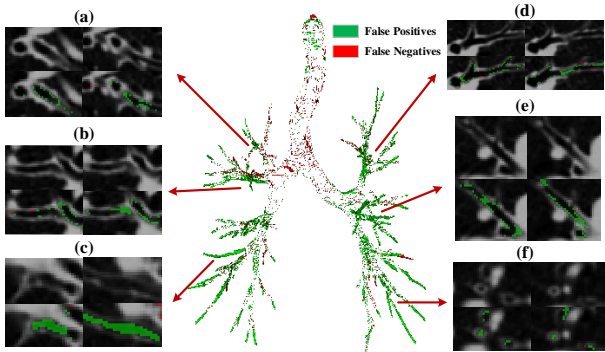


Fig. 9. False positives in the segmentation results. We select six significant regions with false positives and demonstrate the original CT images with the analysis images, in which the false positives are colored in green and the false negatives are colored in red.

growing method. To reduce the leakages, we set the region growing particularly sensitive to these indistinct regions. As a result, such blurry areas were not delineated in the trachea and large bronchi. Moreover, manual annotation could not be perfect for such complicated tree structure and some indistinct regions were annotated to keep the connectivity. During training, these points were emphasized by the focal loss and their patterns were learned by the network. As for the second class of FPs, a small number of the distal small airways with indistinct airway walls were not annotated by the observers, while some of them were detected by our method. The third class is composed of the leakages especially at the bifurcations where the intensities are between airway lumen and walls, as shown in sub-figure (e). In general, the dilation issue in the final segmentation is not as significant as that in the first stage, while the first class of FPs do not affect the clinical use.

### B. False Negatives

We illustrate the false negatives of the failure case with shortest length detected in Fig. 10. Generally, there are two kinds of FNs. The first category can be seen in the indistinct borders between airway lumen and walls. These blurry regions are caused by the limited resolution of CT scans and the

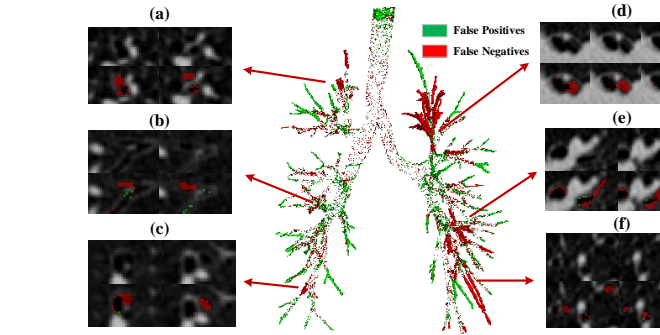


Fig. 10. False negatives in the segmentation results. We select six significant regions with false negatives and demonstrate the original CT images with the analysis images, in which the false positives are colored in green and the false negatives are colored in red.

FNs in these areas do not affect the clinical use. The second class is composed of the undetected branches. As shown in the sub-figures, a common feature of these undetected bronchi is that the intensity distribution of their airway walls is inhomogeneous. In other words, a fraction of the walls are of high intensity while other parts are relatively blurry. These FNs can lead to the breakages, and after extracting the largest connected domain, the rest of a branch is discarded. The network failed to recognize these parts since such pattern was much common in the background. But this also reflects that the network does not learn sufficient long-range features for the connectivity of thin bronchi.

## VII. CONCLUSION

In this paper, we focus on both the inter and intra-class imbalance problems which limit the efficacy of CNNs for distal airway segmentation. With increasing emphasis on early detection and endobronchial intervention, the requirement for complete airway reconstruction at the resolution limit is becoming increasingly important clinically. There is thus far no effective techniques that can address such needs. To deal with inter-class imbalance between foreground and background, we propose the gradient erosion and dilation problem and design a group supervision manner to enhance the training of network.



To resolve the intra-class imbalance between large and small airways, we propose a General Union loss that obviates the impact of airway size by distance-based weights and tunes the gradient ratios of each airway voxel based on the learning process. The proposed method helps to detect more peripheral bronchi, leading to a viable clinical tool for small airway reconstruction and navigation.

## REFERENCES

- [1] N. Abraham and N. M. Khan. A novel focal tversky loss function with improved attention u-net for lesion segmentation. In *2019 IEEE 16th International Symposium on Biomedical Imaging (ISBI 2019)*, pages 683–687, 2019.
- [2] S. Armato, G. McLennan, M. Mcnitt-Gray, C. Meyer, A. Reeves, L. Bidaut, B. Zhao, B. Croft, and L. Clarke. The lung image database consortium (lidc) and image database resource initiative (idri): A completed public database of ct scans for lung nodule analysis. *Medical Physics*, 37(6Part6), 2010.
- [3] C. Bauer, H. Bischof, and R. Beichel. Segmentation of airways based on gradient vector flow. *Second International Workshop on Pulmonary Image Analysis*, pages 191–201, 01 2009.
- [4] S. Born, D. Iwamaru, M. Pfeifle, and D. Bartz. Three-step segmentation of the lower airways with advanced leakage-control. *Second International Workshop on Pulmonary Image Analysis*, pages 239–250, 2009.
- [5] Y. Boykov and M. Jolly. Interactive organ segmentation using graph cuts. In *Medical Image Computing and Computer-Assisted Intervention – MICCAI 2000*, pages 276–286, 2000.
- [6] J.P. Charbonnier, E. Rikxoort, A. Setio, C.M. Schaefer-Prokop, and F. Ciompi. Improving airway segmentation in computed tomography using leak detection with convolutional networks. *Medical Image Analysis*, 36:52–60, 2016.
- [7] Ö. Çiçek, A. Abdulkadir, S. S. Lienkamp, T. Brox, and O. Ronneberger. 3d u-net: Learning dense volumetric segmentation from sparse annotation. In *Medical Image Computing and Computer-Assisted Intervention – MICCAI 2016*, pages 424–432, 2016.
- [8] M. Feuerstein, T. Kitasaka, and K. Mori. Adaptive branch tracing and image sharpening for airway tree extraction in 3-d chest ct. In *Proc of Second International Workshop on Pulmonary Image Analysis*, pages 273–284, 2009.
- [9] R. L. Graham and P. Hell. On the history of the minimum spanning tree problem. *Annals of the History of Computing*, 7(1):43–57, 1985.
- [10] T. Inoue, Y. Kitamura, Y. Li, and W. Ito. Robust airway extraction based on machine learning and minimum spanning tree. In *Medical Imaging 2013: Computer-Aided Diagnosis*, volume 8670, pages 141 – 149. SPIE, 2013.
- [11] B. Irving, P. Taylor, and A. Toddpokropek. 3d segmentation of the airway tree using a morphology based method. In *Proc of Second International Workshop on Pulmonary Image Analysis*, pages 297–307, 2009.
- [12] D. Jin, Z. Xu, A. P. Harrison, K. George, and D. J. Mollura. 3d convolutional neural networks with graph refinement for airway segmentation using incomplete data labels. In *Machine Learning in Medical Imaging*, pages 141–149, 2017.
- [13] A. G. Juarez, R. Selvan, Z. Saghir, and M. de Bruijne. A joint 3d unet-graph neural network-based method for airway segmentation from chest cts. *Machine Learning in Medical Imaging*, 2019.
- [14] A. G. Juarez, H. A. W. M. Tiddens, and M. de Bruijne. Automatic airway segmentation in chest ct using convolutional neural networks. In *Image Analysis for Moving Organ, Breast, and Thoracic Images*, pages 238–250, 2018.
- [15] C. Lee, S. Xie, P. W. Gallagher, Z. Zhang, and Z. Tu. Deeply-supervised nets. *Artificial Intelligence and Statistics*, 2015.
- [16] P. Lo, B.V. Ginneken, J.M. Reinhardt, T. Yavarna, and M.D. Bruijne. Extraction of airways from ct (exact’09). *IEEE Transactions on Medical Imaging*, 31(11), 2012.
- [17] Q. Meng, H.R. Roth, T. Kitasaka, M. Oda, and K. Mori. Tracking and segmentation of the airways in chest ct using a fully convolutional network. In *International Conference on Medical Image Computing and Computer-Assisted Intervention*, 2017.
- [18] F. Milletari, N. Navab, and S. Ahmadi. V-net: Fully convolutional neural networks for volumetric medical image segmentation. In *2016 Fourth International Conference on 3D Vision (3DV)*, pages 565–571, Oct 2016.
- [19] R. Pinho, S. Luyckx, and J. Sijbers. Robust region growing based intrathoracic airway tree segmentation. *Second International Workshop on Pulmonary Image Analysis*, pages 261–271, 01 2009.
- [20] Y. Qin, M. Chen, H. Zheng, Y. Gu, M. Shen, J. Yang, X. Huang, Y. Zhu, and G. Yang. Airwaynet: A voxel-connectivity aware approach for accurate airway segmentation using convolutional neural networks. In *International Conference on Medical Image Computing and Computer-Assisted Intervention*, 2019.
- [21] Y. Qin, Y. Gu, H. Zheng, M. Chen, J. Yang, and Y. Zhu. Airwaynet-se: A simple-yet-effective approach to improve airway segmentation using context scale fusion. In *2020 IEEE 17th International Symposium on Biomedical Imaging (ISBI)*, pages 809–813, 2020.
- [22] A. Rickmann, A. Roy, I. Sarasua, N. Navab, and C. Wachinger. ‘project & excite’ modules for segmentation of volumetric medical scans. In *Medical Image Computing and Computer Assisted Intervention – MICCAI 2019*, pages 39–47, 2019.
- [23] A. Roy, N. Navab, and C. Wachinger. Concurrent spatial and channel ‘squeeze & excitation’ in fully convolutional networks. In *Medical Image Computing and Computer Assisted Intervention – MICCAI 2018*, pages 421–429, 2018.
- [24] S.S.M. Salehi, D. Erdogmus, and A. Gholipour. Tversky loss function for image segmentation using 3d fully convolutional deep networks. *CoRR*, abs/1706.05721, 2017.
- [25] Y. Sato, C. Westin, A. Bhalerao, S. Nakajima, N. Shiraga, S. Tamura, and R. Kikinis. Tissue classification based on 3d local intensity structures for volume rendering. *IEEE Transactions on Visualization and Computer Graphics*, 6(2):160–180, 2000.
- [26] R. E. Schapire and Y. Singer. Improved boosting algorithms using confidence-rated predictions. *Machine Learning*, 37:297–336, 1999.
- [27] C. H. Sudre, W. Li, T. Vercauteren, S. Ourselin, and M. Jorge Cardoso. Generalised dice overlap as a deep learning loss function for highly unbalanced segmentations. In *Deep Learning in Medical Image Analysis and Multimodal Learning for Clinical Decision Support*, pages 240–248, 2017.
- [28] J. Tompson, R. Goroshin, A. Jain, Y. Lecun, and C. Bregler. Efficient object localization using convolutional networks. In *The IEEE Conference on Computer Vision and Pattern Recognition*, pages 648–656, 06 2015.
- [29] C. Wang, Y. Hayashi, M. Oda, H. Itoh, T. Kitasaka, A. Frangi, and K. Mori. Tubular structure segmentation using spatial fully connected network with radial distance loss for 3d medical images. In *International Conference on Medical Image Computing and Computer-Assisted Intervention*, 2019.
- [30] L. Wang, C. Lee, Z. Tu, and S. Lazebnik. Training deeper convolutional networks with deep supervision. *CoRR*, abs/1505.02496, 2015.
- [31] P. Wang and A. C. S. Chung. Focal dice loss and image dilation for brain tumor segmentation. In *Deep Learning in Medical Image Analysis and Multimodal Learning for Clinical Decision Support*, pages 119–127, 2018.
- [32] Y. Wang, Y. Zhou, P. Tang, W. Shen, E. K. Fishman, and A. L. Yuille. Training multi-organ segmentation networks with sample selection by relaxed upper confident bound. In *Medical Image Computing and Computer Assisted Intervention – MICCAI 2018*, pages 434–442, 2018.
- [33] K. C. L. Wong, M. Moradi, H. Tang, and T. Syeda-Mahmood. 3d segmentation with exponential logarithmic loss for highly unbalanced object sizes. *Medical Image Computing and Computer Assisted Intervention*, pages 612–619, 2018.
- [34] Z. Xu, U. Bagci, B. Foster, A. Mansoor, J. K. Udupa, and D. J. Mollura. A hybrid method for airway segmentation and automated measurement of bronchial wall thickness on ct. *Medical Image Analysis*, 24(1):1 – 17, 2015.
- [35] J. Yun, J. Park, D. Yu, J. Yi, M. Lee, H.J. Park, J. Lee, J.B. Seo, and N. Kim. Improvement of fully automated airway segmentation on volumetric computed tomographic images using a 2.5 dimensional convolutional neural net. *Medical Image Analysis*, 51:13 – 20, 2019.
- [36] T. Zhao, Z. Yin, J. Wang, D. Gao, Y. Chen, and Y. Mao. Bronchus segmentation and classification by neural networks and linear programming. In *International Conference on Medical Image Computing and Computer-Assisted Intervention*, 2019.
- [37] Z. Zhou, M. M. Rahman Siddiquee, N. Tajbakhsh, and J. Liang. Unet++: A nested u-net architecture for medical image segmentation. In *Deep Learning in Medical Image Analysis and Multimodal Learning for Clinical Decision Support*, 2018.

## A. Loss Functions

In this section, we provide more detailed analysis about the loss functions used in this paper.

The Dice loss [18] is defined as follows:

$$D = 1 - \frac{2 \times \sum_{i=1}^N p_i g_i}{\sum_{i=1}^N p_i + \sum_{i=1}^N g_i}, \quad (19)$$

where  $N$  is the total number of voxels,  $p_i$  is the prediction of each voxel and  $g_i$  is the corresponding ground truth. It is differentiated in terms of  $p_j$ , and the gradient is

$$\frac{\partial D}{\partial p_j} = -2 \left[ \frac{g_j \left( \sum_{i=1}^N p_i + \sum_{i=1}^N g_i \right) - \sum_{i=1}^N p_i g_i}{\left( \sum_{i=1}^N p_i + \sum_{i=1}^N g_i \right)^2} \right]. \quad (20)$$

It can be seen that the same gradients are given to all foreground or background locations ( $\frac{\partial D}{\partial p_i} = \frac{\partial D}{\partial p_j}$  if  $g_i = g_j$ ). For further analysis with regard to the gradient erosion and dilation, we calculate the ratio of the foreground gradient  $\frac{\partial D}{\partial p_f}$  to background gradient  $\frac{\partial D}{\partial p_b}$ ,

$$\begin{aligned} r_{Dice} &= \left| \frac{\partial D}{\partial p_f} / \frac{\partial D}{\partial p_b} \right| = \frac{\sum_i (p_i + g_i) - \sum_i p_i g_i}{\sum_i p_i g_i} \\ &= \frac{2}{1 - D} - 1. \end{aligned} \quad (21)$$

This proportion is in inverse ratio to the Dice similarity coefficient (DSC). During training, if an input patch includes both small and large airways, the total DSC is high as the large airways are not seriously influenced by the inter-class imbalance. This leads to small  $r_{Dice}$  which aggravates the gradient erosion, thus affecting the learning of small airways. To improve the airway tree length detected, we can impose a lower bound to the gradient ratio, preventing the gradient erosion problem. This can be achieved by weighted Dice loss and Tversky loss [24].

For weighted Dice loss,

$$D_w = 1 - \frac{2 \times \sum_{i=1}^N w_i p_i g_i}{\sum_{i=1}^N w_i (p_i + g_i)}, \quad (22)$$

it is differentiated in terms of  $p_j$ , and the gradient is

$$\frac{\partial D_w}{\partial p_j} = -2 \frac{w_j g_j [\sum_{i=1}^N w_i (p_i + g_i)] - w_j \sum_{i=1}^N w_i p_i g_i}{[\sum_{i=1}^N w_i (p_i + g_i)]^2}. \quad (23)$$

Similar to Dice loss, the same gradients are given to all foreground or background voxels ( $\frac{\partial D_w}{\partial p_i} = \frac{\partial D_w}{\partial p_j}$  if  $g_i = g_j$ ). Its gradient ratio is

$$\begin{aligned} \left| \frac{\partial D_w}{\partial p_f} / \frac{\partial D_w}{\partial p_b} \right| &= \frac{w_f \sum_i w_i (p_i + g_i) - w_f \sum_i w_i p_i g_i}{w_b \sum_i w_i p_i g_i} \\ &= \frac{w_f}{w_b} \left( \frac{2}{1 - D_w} - 1 \right) \geq \frac{w_f}{w_b}, \end{aligned} \quad (24)$$

where  $w_f$  and  $w_b$  are the weights for foreground and background respectively. From Eq. (24), we can find three properties of weighted Dice loss. First, its gradient ratio can be adaptively changed due to the item  $\frac{2}{1 - D_w} - 1$ . Second, this change is amplified by the factor  $\frac{w_f}{w_b}$ . Third, the gradient ratio

has a lower bound of  $\frac{w_f}{w_b}$ . These properties make it effective to improve the segmentation by tuning the weights  $w_f$  and  $w_b$ .

The same properties can be found in Tversky loss,

$$T = 1 - \frac{\sum_{i=1}^N p_i g_i}{\sum_{i=1}^N p_i g_i + \alpha \sum_{i=1}^N p_i (1 - g_i) + \beta \sum_{i=1}^N (1 - p_i) g_i}, \quad (25)$$

where  $\alpha + \beta = 1$ , so it can be rewritten as

$$T = 1 - \frac{\sum_{i=1}^N p_i g_i}{\sum_{i=1}^N (\alpha p_i + \beta g_i)}. \quad (26)$$

Its gradient can be calculated by

$$\frac{\partial T}{\partial p_j} = - \frac{g_j \sum_{i=1}^N (\alpha p_i + \beta g_i) - \alpha \sum_{i=1}^N p_i g_i}{[\sum_{i=1}^N (\alpha p_i + \beta g_i)]^2}, \quad (27)$$

and the gradient ratio is

$$\begin{aligned} \left| \frac{\partial T}{\partial p_f} / \frac{\partial T}{\partial p_b} \right| &= \frac{\sum_{i=1}^N (\alpha p_i + \beta g_i) - \alpha \sum_{i=1}^N p_i g_i}{\alpha \sum_{i=1}^N p_i g_i} \\ &= \frac{1}{\alpha} \frac{1}{1 - T} - 1 \geq \frac{\beta}{\alpha}. \end{aligned} \quad (28)$$

By tuning the importance of false positives and false negatives in the denominator, Tversky loss also can achieve a high sensitivity for peripheral small airways.

Despite the merits of these losses, they do not address the intra-class imbalance problem. The cost for a high tree length detected is the significant dilation problem, because the same large gradients are assigned to all foreground points. Actually, we do not need to increase the gradients to the easy-to-segment parts such as the large airways, while more attention should be paid to the hard-to-segmentation areas to improve the connectivity of the predicted bronchi. To this end, we propose a Root Tversky loss which combines the voxel-level focal function into Tversky loss, and a General Union loss is further generated by adding the distance-based weights.

Root Tversky loss achieves the element-wise focal function by changing the root of the predictions in the numerator of Tversky loss,

$$T_r = 1 - \frac{\sum_{i=1}^N p_i^r g_i}{\alpha \sum_{i=1}^N p_i + \beta \sum_{i=1}^N g_i}, \quad (29)$$

where  $0 < r < 1$  and  $\alpha + \beta = 1$ . It is differentiated in term of  $p_j$ , and the gradient is

$$\frac{\partial T_r}{\partial p_j} = - \frac{r g_j p_j^{r-1} (\alpha \sum_{i=1}^N p_i + \beta \sum_{i=1}^N g_i) - \alpha \sum_{i=1}^N p_i^r g_i}{(\alpha \sum_{i=1}^N p_i + \beta \sum_{i=1}^N g_i)^2}. \quad (30)$$

As  $r - 1 < 0$ , we replace  $p_j^{r-1}$  by  $(p_i + \epsilon_i)^{r-1}$  where  $\epsilon_i$  is a small positive number. The same gradients are given to all background voxels while  $p_j^{r-1}$  controls the gradients given to foreground locations. Since  $0 < r < 1$ , much larger gradient is given to the foreground voxel with small  $p_j$ . Its gradient ratio is

$$\begin{aligned} \left| \frac{\partial T_r}{\partial p_f} / \frac{\partial T_r}{\partial p_b} \right| &= \frac{r p_{f,j}^{r-1} (\alpha \sum_{i=1}^N p_i + \beta \sum_{i=1}^N g_i) - \alpha \sum_{i=1}^N p_i^r g_i}{\alpha \sum_{i=1}^N p_i^r g_i} \\ &= \frac{r p_{f,j}^{r-1}}{\alpha} \frac{1}{1 - T_r} - 1 \geq \frac{r}{\alpha} - 1, \end{aligned} \quad (31)$$

where  $p_{f,j}$  is the prediction of a foreground voxel  $j$ . Comparing Eq. (28) and (31), the main difference between Tversky loss and Root Tversky loss is that the amplification factor  $\frac{1}{\alpha}$  in Tversky loss is replaced by  $\frac{rp_{f,j}^{r-1}}{\alpha}$ . In this new factor, the  $p_{f,j}^{r-1}$  item achieves the voxel-wise focal function for the hard-to-segment points, while for the easy-to-segmentation airway voxels, this factor is near  $\frac{r}{\alpha}$ , resulting in smaller gradient ratio and alleviating the dilation problem.

As the intra-class imbalance is caused by the large number of thick airway voxels, we can manually decrease the weights for most large airway points. In this paper, we achieve this by assigning the weights for each voxel according to their distance to the centerlines,

$$w_i = \begin{cases} 1 - m \left( \frac{d_i}{d_{max}} \right)^{r_d}, & g_i = 1 \\ 1, & g_i = 0 \end{cases} \quad (32)$$

where  $d_i$  is the shortest distance from the current location to the centerline,  $d_{max}$  is the maximum  $d_i$  in one case and  $r_d$  controls the pattern of decay. By adding this weight to Eq. (31), the loss function is in the following form:

$$U = 1 - \frac{\sum_{i=1}^N w_i p_i^{r_l} g_i}{\sum_{i=1}^N w_i (\alpha p_i + \beta g_i)}. \quad (33)$$

To reduce the number of hyper-parameters, we set  $m = \frac{1-\alpha}{\alpha}$  in  $w_i$ . Its gradient with regard to  $p_j$  is

$$\frac{\partial U}{\partial p_j} = - \frac{w_j r g_j p_j^{r-1} \sum_i w_i (\alpha p_i + \beta g_i) - w_j \alpha \sum_i w_i p_i^r g_i}{[\sum_{i=1}^N w_i (\alpha p_i + \beta g_i)]^2}. \quad (34)$$

And the gradient ratio of this loss is

$$\begin{aligned} \left| \frac{\partial U}{\partial p_f} / \frac{\partial U}{\partial p_b} \right| &= \frac{w_{f,j} r p_{f,j}^{r-1} \sum_i w_i (\alpha p_i + \beta g_i) - w_{f,j} \alpha \sum_i w_i p_i^r g_i}{\alpha \sum_i w_i p_i^r g_i} \\ &= w_{f,j} \left[ \frac{r p_{f,j}^{r-1}}{\alpha} \frac{1}{1-U} - 1 \right] \\ &\geq (1-m) \left( \frac{r}{\alpha} - 1 \right). \end{aligned} \quad (35)$$

It is seen that the distance-based weight  $w_i$  is directly applied on the gradient ratio of each point. Besides, since the weights of most large airway voxels are decreased, small airways play a more important role in the item  $\frac{1}{1-U}$ . In other words, the adaptive changing of gradient ratio depends more on the sensitivity of peripheral bronchi. By adopting this distance-based weight, the dilation issue around the large airways can be resolved while keeping a high tree length detected.

## B. Hyper-parameters

Actually, our method includes some hyper-parameters, and the selection of these parameters is a time-consuming project. To provide a clear illustration of their impacts, in this section, we set experiments on the Binary Airway Segmentation dataset to analyze each of them. We demonstrate the performance in two training stages. In the first stage, the network is forced to achieve a high tree length detected, while in the second stage, the model is fine-tuned to increase the precision

of segmentation. In this following experiments, the network was trained by General Union loss in the first stage, while Root Tversky loss was used in the second stage.

## C. $r_l$ in GUL/RTL

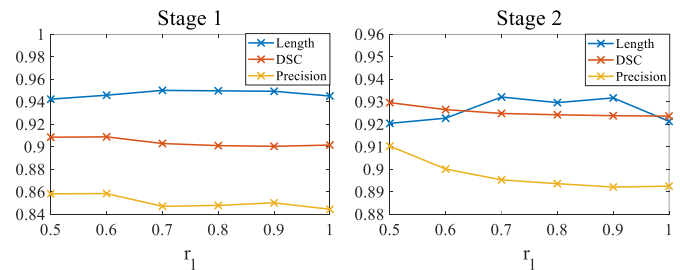


Fig. 11.  $r_l$  is the root of the prediction in the numerator of GUL/RTL, which controls the extent of the focal function. It also impacts the gradient ratio and a small  $r_l$  can alleviate the dilation issue.

The hyper-parameter  $r_l$  in GUL or RTL is the root of the predictions in the numerator, which controls the extent of the element-wise focal function. Loss function with smaller  $r_l$  focuses more on the failure locations. Moreover, smaller  $r_l$  leads to a smaller amplification factor of the gradient ratio. Therefore, as shown in Fig. 11, the precision drops as  $r_l$  rises. Besides, the excessive focus on the failure points is not beneficial to detect more small airways. In both stages, the length detected of the results of  $r_l = 0.5$  is slightly worse than the results of  $r_l = 1.0$ . In contrast, a moderate focal effect helps the network learn better representations for peripheral bronchi.

## D. $r_d$ in GUL

The hyper-parameter  $r_d$  in GUL controls the speed of the distance-based weight decay of airway voxels. In this experiment, we evaluated three decay modes as shown in Fig. 12,  $r_d = 0.5$ ,  $r_d = 1.0$  and  $r_d = 2.0$ . When  $r_d = 0.5$ , the weight decreases fast around the centerline. A linear decay is achieved by  $r_d = 1.0$  and  $r_d = 2.0$  can keep a high weight around the centerline. In the first stage, all the modes can yield a high length detected while  $r_d = 0.5$  performs better than others for the gradient dilation problem. In the second stage, paying more attention to the centerlines can improve the length detected. Therefore, we chose  $r = 0.5$  in other experiments.

## E. $\alpha_e$ and $\alpha_d$

In WingsNet, two loss functions are imposed on the encoding group and decoding group respectively. To evaluate different combinations of the hyper-parameters  $\alpha_e$  and  $\alpha_d$  in these two loss functions, we fix one parameter while varying another one in both stages. As shown in Fig. 13, since we use the predictions of the decoding group as the final results, the trade-off between sensitivity and specificity is mainly controlled by  $\alpha_d$ . Smaller  $\alpha_d$  results in a higher amplification factor of the gradient ratio, alleviating the gradient erosion and improving the length detected. In contrast, the impact of  $\alpha_e$  is

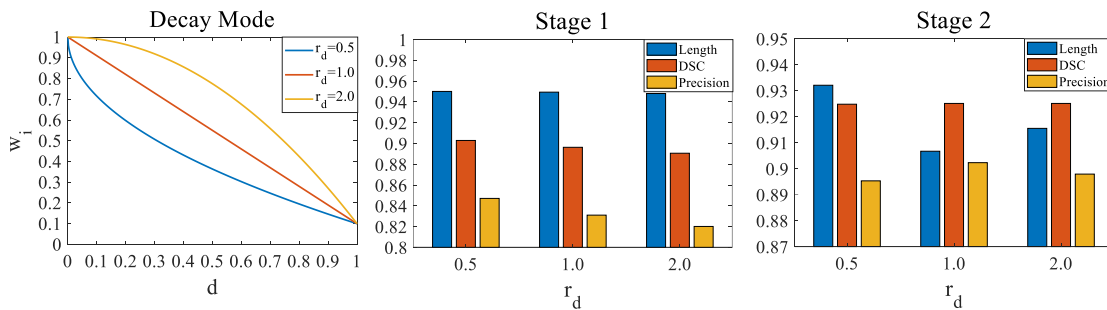


Fig. 12.  $r_d$  is the root of the relative distance in GUL, which decides the speed of the distance-based weight decay of airway voxels.

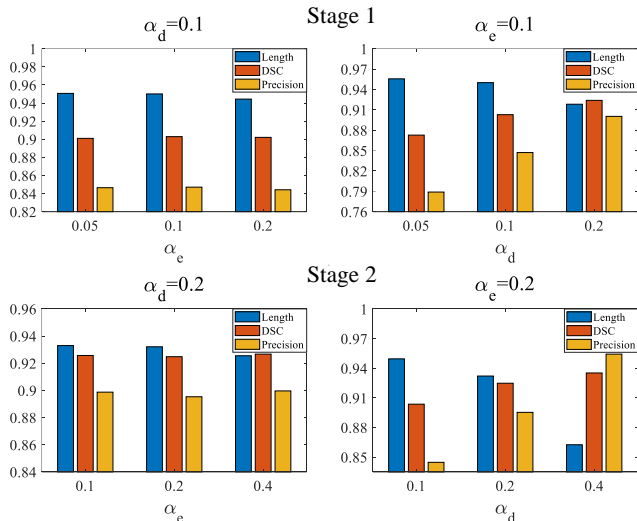


Fig. 13.  $\alpha_e$  and  $\alpha_d$  are the hyper-parameters in GUL/RTL imposed on the encoding group and decoding group respectively. The final segmentation performance is mainly affected by  $\alpha_d$ . Small  $\alpha$  leads to high gradient ratio, improving the length detected while decreasing the precision.

insignificant in the first stage, while in the second stage, a large  $\alpha_e$  reduces the length detected. In test set, the combination of  $\alpha_e = 0.1$  and  $\alpha_d = 0.2$  achieves the best results in the second stage. However, in validation set, the optimal selection is  $\alpha_e = \alpha_d = 0.2$ . Thus, in other experiments, we chose  $\alpha_e = \alpha_d = 0.1$  in the first stage and  $\alpha_e = \alpha_d = 0.2$  in the second stage.

### F. $p_d$ in SpatialDropout

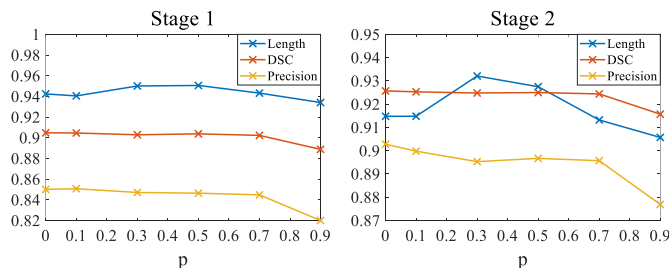


Fig. 14.  $p_d$  in SpatialDropout controls the probability of each channel to be dropped. Small  $p_d$  can improve the generalization while large  $p_d$  affects the learning of hierarchical representations.

When performing SpatialDropout, a hyper-parameter  $p_d$  is set to control the probability of each channel to be dropped. As shown in Fig. 14, a suitable  $p_d$  helps the network to learn robust features for the distal small airways, improving the length detected. However, when  $p_d$  is greater than 0.5, both the length detected and precision drop as  $p_d$  increases. In this case, the prediction only relies on several layers, which is a little like the deeply supervised nets, limiting the learning of hierarchical representations. When choosing this hyper-parameter,  $p_s = 0.3$  achieves the best length detected in the second stage in both the validation set and test set. Besides, our method performs stably within the interval of  $[0.3, 0.5]$ . Thus, we selected  $p_d = 0.3$  in other experiments.

### G. Threshold in Data Augmentation

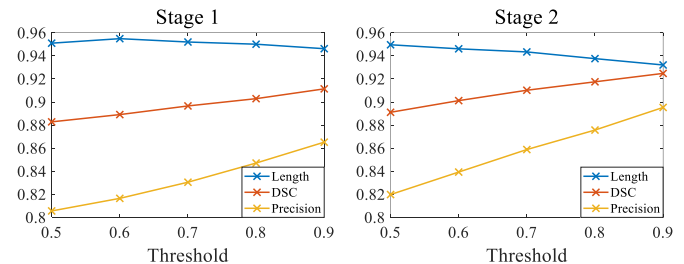


Fig. 15. Threshold in data augmentation. This parameter affects the thickness of small airway annotations after random rotation. A large threshold slightly decreases the length detected while improving the precision.

In data augmentation, the threshold of interpolation directly affects the thickness of small airway annotations after random rotation. A small threshold can enlarge the bronchi annotations, which is beneficial to detect more small airways but leads to more serious dilation problem. As shown in Fig. 15, the opposed trends are seen in the lines of length detected and precision. To improve the precision of our results, we chose a pretty high threshold (0.9) in the second stage while slightly decreasing this number to 0.8 for higher sensitivity in the first stage.

### H. $p_s$ in Data Sampling

During training, a probability  $p_s$  is set to perform hard skeleton sampling or random sampling. As shown in Fig. 16, in the first stage, adopting hard skeleton sampling can improve the length detected about 1%, and this margin is more

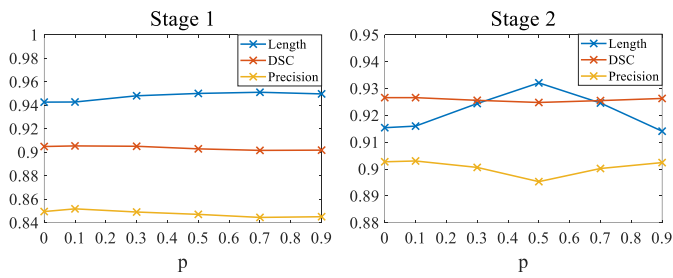


Fig. 16. During training, a probability  $p_s$  is set to perform hard skeleton sampling or random sampling. Adopting hard skeleton sampling can boost the length detected while the overuse inversely affects the performance.

significant (about 2%) in the second stage. It is also seen that a pretty high  $p_s$  leads to the decrease in both length detected and precision. In this case, the model over-fits to these difficult regions, affecting the generalization capability. Therefore, we selected  $p_s = 0.5$  in other experiments.